Chapter 7

Pulsed laser deposition of thin oxide films. Application in electrochemistry

M. J. Montenegro, T. Dumont, T. Lippert, S. Müller[a], A. Weidenkaff[b], A. Wokaun

Paul Scherrer Institut, CH-5232 Villigen PSI, Switzerland
[a]Euresearch, Effingerstr. 19 CH-3001, Bern, Switzerland
[b]Empa, CH- 8600 Dübendorf, Switzerland

The pulsed reactive crossed-beam laser ablation (PRCLA) is discussed in relation with the preparation of thin films of perovskite-type oxide materials without oxygen deficiencies and without additional processing steps (e.g. annealing).

Introduction

Metal oxides

Metal oxides constitute a fascinating class of materials whose properties cover the entire range from metals to semiconductors and insulators. Their surfaces play a crucial role in several processes, i.e. passivation of metal surfaces against corrosion, catalysis for the partial oxidation of hydrocarbons, and the stability of electrode/electrolyte interfaces in fuel cells.

In spite of all their technological and scientific importance, our understanding of the basic physics and chemistry of metal-oxide surfaces lags a decade or more behind that of other metals and semiconductors. The main reasons are related to the complexity of their structures and properties. Transition metals display a range of possible oxidation states and hence a series of oxides with different compositions and chemical/physical properties. There exists a pronounced difficulty to reproduce samples with the same composition and properties. Adding the fact, that surfaces with the apparently same composition, but prepared slightly different, can present completely different properties. The electronic structure adds an additional point to the complexity. For example, the $La_{1-x}Ca_xMnO_3$ bulk electronic structure exhibits a competition between localized into itinerant electrons and none of the existing models is entirely appropriate.

However, over the past twenty years, an increasing number of groups have begun to study the properties of transition metal oxides for novel applications. For example in catalysis stimulated by the discovery of TiO_2 as a catalytic electrode in

a photoelectrolysis cell, which decomposes water into H_2 and O_2, without the application of an external voltage [1] or by the discovery of Cu-oxide-based high T_c superconductors [2].

Perovskite the "inorganic chameleon"

Metal oxides, with an empirical formula ABO_3, derive their name from the mineral "perovskite", with the chemical structure $CaTiO_3$. The cubic form of this material is referred to as ideal perovskite, and has a unit cell edge of approximately 4Å. In reality, only a few perovskite-type materials have this ideal cubic structure at room temperature, but many reach it at higher temperatures [3]. Distortions from the cubic symmetry produce tetragonal, orthorhombic, and rhombohedral structures as shown in Fig. 1. In the face centred cubic (FCC) structure the *A cations* are located at the corners while the O atoms are on the faces. The *B cation* is in the centre of the unit cell.
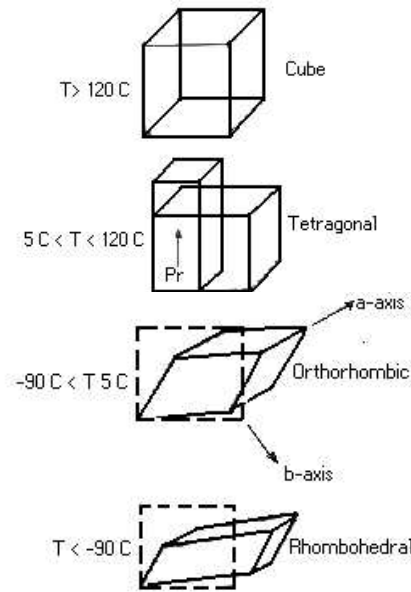

Fig. 1. Different perovskite structures.

.

A tolerance factor *t* was defined by Goldschmit [4] to describe the stability limits of the perovskite structure (Eq. (1)).

$$t = (R_A + R_O) / 2^{1/2} (R_B + R_O) \qquad (1)$$

where R_A, R_B and R_O are the ionic radii. The perovskite is stable within the range of $0.75 < t < 1.0$ with *t* normally between 0.8 and 0.9. The stable structures below this limit are ilmenite and corundum [5]. The perovskite structure possesses a very high degree of compositional flexibility, which allows to accommodate a wide variety of A and B cations, and is also tolerant for large concentrations of both oxygen and cation vacancies. In some complex composition the A and B sites can be occupied by more than one cation species ($A_{1-x}A'_xB_{1-y}B'_yO_3$). In the case of the

B sites this can involve cations of more than one element (chemical variation), or different oxidation states of the same element (charge variation).

Perovskite is one of the most important structure classes in material science due to a plethora of exceptional physical and chemical properties. The physical properties of the perovskite-type materials, such as ferroelectric, dielectric, pyroelectric, and piezoelectric behaviour, will depend on the cation ordering, anion vacancies, and changes in the structural dimensionality. In addition to these physical properties numerous important chemical properties are observed, including catalytic activity and oxygen transport capability. The catalytic activity covers reactions such as CO oxidation, NO reduction, CO and CO_2 hydrogenation, SO_2 reduction and various electro-photocatalytic reactions [6]. Some perovskites, i.e. $La_{1-x}Sr_xMnO_3$,

$La_{1-x}Sr_xCo_{1-y}Fe_yO_3$, $SrCeO_3$ and $SrTiO_3$ are used for oxygen transport applications (e.g. in gas diffusion electrodes). The ongoing research does not only cover the study of magnetic and electronic properties [7], but also the development of new materials to optimize renewable energy sources, i.e. solid oxide fuel cells [8], direct methanol fuel cells, and metal/air batteries [9].

The most important topic for the production of metal/air batteries (i.e. Zn/air) is the development of new materials for anodes and cathodes. These materials have to be stable under long term operation conditions (acidic or alkaline medium with an applied potential), and should be cheaper than the commonly used noble metal materials, i.e. Pt.

The first Zn air battery employing an alkaline electrolyte was patented in 1894, and consisted of a central Zn electrode, a porous separator, an inner fine particulate carbon layer, an outer particulate carbon layer, and a perforated Ni current collector. Cells of this type have capacities in the range from 300 to 3000 Ah, with a specific power of less than 1 W/l. Recently, the interest in this type of battery was renewed, as many technical problems could be solved and batteries of this type became commercially available. The Zn air battery is the battery that offers one of the highest storage densities, which is due to the fact that one of the components in the reaction comes from outside of the battery, i.e. atmospheric oxygen from the air as cathode reactant. A primary Zn air battery is also characterized by a long shelf life when sealed, e.g. a loss of only $\approx 2\%$ of its capacity is experienced after one year of storage (for a cell voltage of 1.65 V).

The recent design of a re-chargeable Zn air battery consists of two electrodes, i.e. Zn paste and a bifunctional oxygen electrode with an integrated electrocatalyst for reduction and evolution of oxygen [10, 11].

However, one major problem associated with the development of these secondary batteries is the limited lifetime of the bifunctional electrode (which catalyzes the reduction and the evolution of oxygen). The lifetime of this electrode is controlled by the dissolution of the catalyst in the electrolyte [12] and the corrosion of the support material (carbon). Progress has been made in the development of corrosion resistant carbon, e.g. carbon nanotubes [13] as support material for the electrodes [14]. Nevertheless, the development of a stable catalyst is still a challenging task. Only few catalysts are intrinsically bifunctional to act as catalysts for both oxygen reactions. Most of the catalysts exhibit either a low catalytic activity or they are unstable under operating conditions [15, 16]. Various catalysts such as noble metals [17], perovskites, spinel, pyrochlore type oxides [18-20], organometallic compounds [21], and other materials [22] have been evaluated

and various methods have been developed to prepare catalytic powders with high surface areas [23]. In particular, the perovskites containing Co, Fe, Mn and Ni are excellent catalysts for the oxygen evolution (OER) and oxygen reduction reaction (ORR) [24, 25].

The origin of the catalytic activity is not yet fully understood, but several hypothesis have been suggested i) a relation between the catalytic activity and the density of states at the Fermi level [26]; ii) the influence of the metal-oxygen binding energy and the π back bonding from the oxygen to the neighbouring cations [27]; iii) the presence of oxygen vacancies [28, 29] and iv) that electrical conductivity and magnetic properties are important [26]. Different mechanisms have also been proposed for the oxygen reduction/evolution reactions with perovskite-type oxides as catalysts, but contradictory results have been published [30, 31]. This is most probably due to the different preparation methods for the catalysts powder and the electrodes.

The best method to overcome this influence is the preparation of electrodes on inactive substrates with well defined electrolyte/oxide interfaces, i.e. model system. This will allow to study and compare the mechanism of the oxygen reduction/evolution reaction of different perovskite oxides without any interference from the carbon support material. These interferences are electrochemical activity and stability of the carbon, and the uncertainty about the real area of the electrode due to the porous structure. Another advantage of the model system is the possibility to study the influence of the crystallographic orientation on the catalytic activity. The best model system will therefore be a dense crystalline films deposited on an inactive substrate.

Lithium spinels as cathode material in lithium batteries

Another class of oxides that play a major role for batteries, but in the case of lithium-batteries, are lithium spinels. The ideal spinel oxide structure is AB_2O_4 where the oxygen atoms form a face-centered cubic packing and occupy 32e sites of the space group Fd3m. The cations A and B occupy the tetrahedral 8a sites and the 16d sites respectively, whereas the octahedral site 16c remains empty. The spinel structure is illustrated in Fig. 2. For cathode electrode materials, suitable lithium spinels oxides are generally of the form LiM_2O_4 (with M: transition Metal such as Mn and Co). The 8a tetrahedral and 16c octahedral sites of the Mn_2O_4 framework form a diamond type network. The empty sites are interconnected by common faces and edges to form a three-dimensional pathway for the lithium diffusion (see Fig. 2, right). The angles formed by the consecutive straight spokes, 8a - 16c - 8a measure about 107°. In the case of $LiMn_2O_4$, the lattice constant of the unit cell is 8.247 Å. However, in inverse spinels, where a part of the transition metal ions situated in the 16d sites displace the lithium ions in the 8a sites and prevent easier diffusion of lithium ions from 8a to other 8a sites via vacant octahedral 16c sites. The lithium intercalation has long been demonstrated for LiM_2O_4 (with M= Ti, V, Mn) with a capacity of one additional lithium atom per formula unit at room temperature [32-37]. In addition to that, some studies were carried out on more complex spinel type phases such as $Li_2Mn_4O_9$, $Li_4Mn_5O_{12}$, $Li_4Ti_5O_{12}$, $LiFe_5O_8$, etc [38-41].
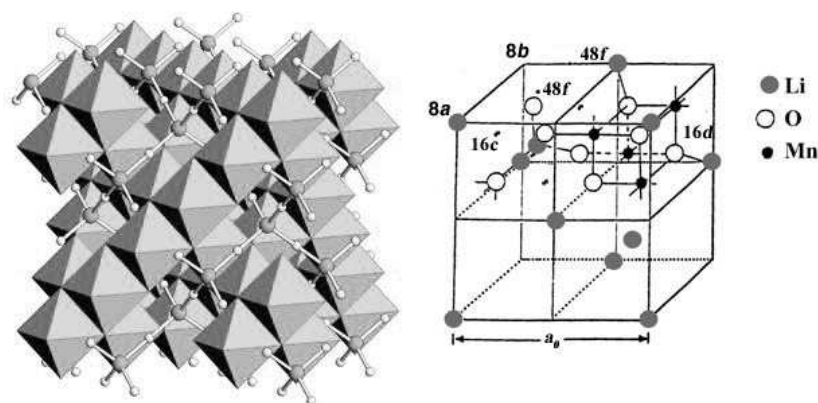
Fig. 2. Crystal structure of spinel phase, general (left) and for LiMn₂O₄ (right. Adopted from [42]).

During charge and discharge of the battery, the lithium ions are extracted and reintercalated respectively into the spinel framework. In Fig. 3 a typical cyclic voltammogram in the 3.4 to 4.5 V range of a LiMn$_2$O$_4$ film produced by PLD onto stainless steel substrates is shown. The four peaks correspond to the intercalation/deintercalation of the Li-ions into the spinel phase. The first step is usually located between 3.9 and 4.1 V (in this case at 4.03 V). It corresponds to the extraction of lithium from half of the tetrahedral sites during charging. The second peak is situated between at 4.17 V and corresponds to the extraction from the rest of the Li ions. The Li-Li interaction forces are much stronger after extraction of the first part of the Li-ions due to the formation of Mn^{4+} sites. Extraction of Lithium from sites in the neighborhood of Mn^{4+} sites requires more energy, which is the reason for the pronounced two steps Li extraction. The two peaks at 3.99 and 4.1 V (at negative currents) correspond to the reintercalation of lithium upon discharge.
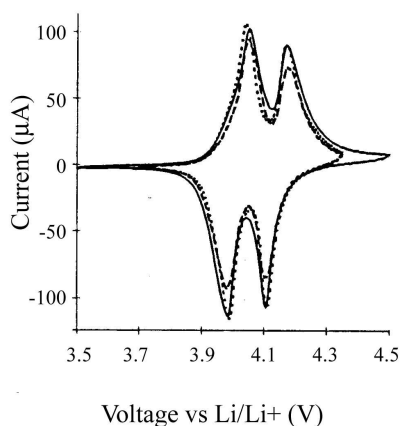

Fig. 3. Cyclic voltammogram of three 0.3 μm thick LiMn$_2$O$_4$ in 1M LiPF$_6$/EC/DMC (1:2), 1 mV/s. adopted from [43].

211

Deposition techniques for thin film electrodes

Several techniques such as molecular beam epitaxy (MBE) [44], chemical vapor deposition (CVD) [45], sputtering (RF, Magnetron, and ion beam) [46], and pulsed laser deposition (PLD) [47-49] have been used to deposit thin films. The advantages of PLD compared with other deposition techniques are well summarized by Chrisey and Hubler [50]. Briefly, the main advantage of PLD is the flexibility to control different parameters which allows an optimization of the deposition conditions. The arrival rates of atoms on the substrate and the possibility to work with higher pressures of background gases are other important factors. PLD has been successfully used for the growth of many types of multicomponent thin films with a very high quality [51, 52]. Nevertheless, some limitations exist, such as particulates, incongruent ablation and oxygen deficiency in oxide materials. To minimize these limitations some modifications to the traditional PLD method have been developed. Some examples for these modifications are Aurora-PLD [53], RF plasma assisted pulsed laser deposition [54, 55], PLD with an electric field applied to the substrate [56], UV assisted PLD [57], off-axis PLD [58], magnetic-field PLD [59], and pulsed reactive crossed-beam laser ablation (PRCLA) [60].

The first report on the combination of a pulsed gas supply with PLD was published by Gupta and Hussey in 1991 [61]. This setup allows the application of low background pressures, which enables the implementation of in situ vacuum characterization techniques, e.g. reflection high-energy electron diffraction (RHEED). The main difference between this setup and the PRCLA setup used in our studies (Fig. 4) is the distance of the gas pulse to the ablation spot on the target.
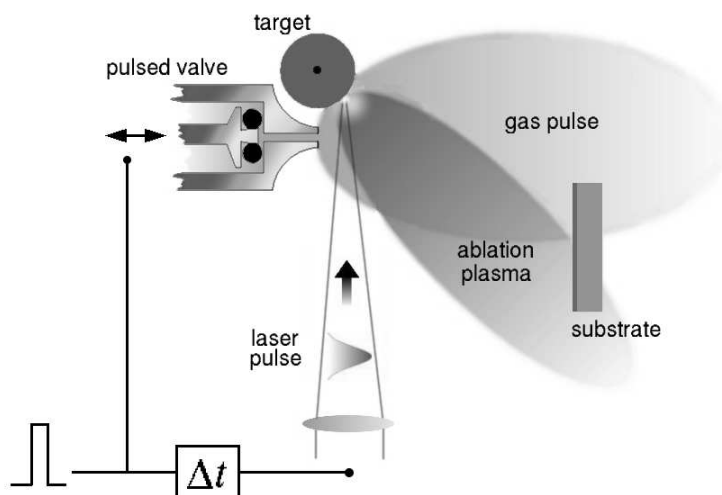

Fig. 4. Pulsed reactive cross-beam laser deposition setup.

For PRCLA the distance is smaller than 10 mm, which allows an increase of the gas phase interaction and the probability of reactive scattering between the gas pulse and plasma, while the resulting species propagate freely away from the

localized scattering region [51]. The advantages of PRCLA compared to PLD were demonstrated by Willmott and Antoni [62] for the growth of GaN films. PRCLA has also been applied successfully [63] for the growth of perovskite films. The films present the desired oxygen content without any post-annealing procedure.

The optimization of the different deposition parameters during the growth of $La_{0.6}Ca_{0.4}CoO_3$ thin films, and its influence on the electrochemical performance for the oxygen evolution/reduction reaction, are presented in this chapter. The specific material composition was selected due to its industrial application as bifunctional catalyst in electrically rechargeable Zn/air batteries [20, 64, 65].

Experimental

Thin films of $La_{0.6}Ca_{0.4}CoO_3$ were deposited by ablation of a rotating rod target, which was sintered from powders prepared by spray pyrolysis at Praxair Surface Technology. The stoichiometry of the target (i.e. $La_{0.6}Ca_{0.4}CoO_3$) was confirmed by atomic emission spectroscopy. A KrF excimer laser ($\lambda = 248$ nm) with a pulse duration of 17 ns was used as irradiation source. The target material is located by default at a distance of 4.5 cm from the substrate, but this distance can be varied if necessary. The target was ablated with a laser fluence of 7.6 Jcm^{-2} at a repetition rate of 10 Hz with 21,000 pulses for each film.

The films were grown on MgO(100),(110),(111), and stainless steel (Cr-Ni, type SUS 304, $10 \times 10 \times 0.5$ mm^3) substrates with one side polished and at a typical temperature of 650 °C (for some experiments this value was changed). The substrates were heated by clamping them to Si substrates, where the rough sides of both were in contact. The Si substrates were ohmically heated by passing a DC current through them. The temperature of the Si substrates was determined by monitoring the resistivity of the Si wafer, which can be compared to reference tables [66]. The substrates were rotating during the deposition to obtain uniform ablation thickness.

Two different oxygen sources were used during film growth, i.e. from a synchronized pulsed valve operating at a backing pressure p of 2 bar N_2O (99.999 % purity, pulse length of 400 µs) and a leak valve to provide an additional background pressure of O_2 of $p \approx 8 \times 10^{-4}$ mbar during the deposition. The time delay between the gas pulse and the laser pulse was 400 µs, at which the maximum interaction between the ablation plasma and the gas pulse is achieved, as described in detail elsewhere [51]. The films were cooled with a "fast procedure" after the deposition, where the chamber was vented and the films were removed after 15 minutes (≈ 40 °C/min cooling rate). The film thickness and surface roughness were determined with a profilometer (Dektak 8000). The topography of the films was also measured with an Atomic Force Microscope (AFM) from Park Scientific Instrument, in contact mode. The crystalline structure and texture of the films were determined by a Siemens D5000 X-ray diffractometer with Bragg-Brentano geometry using Cu Kα radiation. The apparatus is equipped with an Eulerian cradle for sample orientation. The tubular aperture is limiting the beam divergence of 0.3°. Scans in $\theta/2\theta$ geometry under different tilt angles were performed using an aperture of 0.2 mm. The film stoichiometry was determined by Rutherford

Backscattering Spectroscopy (RBS) measurements using a 2 MeV [4]He beam and a surface barrier silicon detector. The collected data were analyzed using the RUMP program [67].

The preparation of the gas diffusion electrodes has been described in detail previously [68]. The electrochemical activity of the LCCO films and gas diffusion electrodes for the oxygen reactions was measured with a three electrodes arrangement with the LCCO as a working electrode, a Pt-wire as counterelectrode, and an Hg/HgO as reference electrode with a potentiostat (Amel instruments, model 2049). The electrodes are submerged in a cell with a 1M solution of KOH. Oxygen is bubbled for saturation through the KOH solution. A potential is applied to the electrode, obtaining the current as an answer, which is normalized for the electrode area (i.e. current density).

Results and discussion

Parameter which influence thin film growth of perovskites

When PLD is performed under vacuum conditions, two main aspects are different from sputtering or conventional thermal evaporation techniques. First, pulses of high vapour fluxes (~ 1 ms) are separated by periods of no vapour flux (~ 100 ms) and relatively high vapour arrival energies at the substrate. Second, there are ions with energies in the keV range and neutral atoms with energies of several eV.

When PLD is performed in the presence of oxygen as background gas, two effects are expected during the film formation: i.e. the reduction of the kinetic energy of the vapour flux, and ii. it provides a high flux of background oxygen molecules bombarding the surface during deposition. This high flux could change the film and substrate surface energies and will increase the oxygen content (for the oxide films).

The first arriving pulse causes the nucleation of a high density of smaller clusters. These subcritical clusters tend to dissociate into mobile species that will nucleate new clusters of a different size during the time of no vapour arrival. The next pulse will initiate the same process again, with the difference that some of the mobile atoms will reach the previous formed clusters.

There are a number of changes in the film growth mode that are readily observed as a function of the PLD parameters (wavelength, fluence, repetition rate, and pulse width). Table 1 presents a summary of different deposition parameters and the effect on the film growth [50].

Table 1. Relationship between deposition parameters and film characteristics.

Category	Parameters	Effect on process	Possible effect on film
Primary	Laser Wavelength Laser Power Density	Thermal or nonthermal evaporation	Control of compositional variation and transfer ratio
	Laser Repetition Rate	Ratio of neutral to ionic species in the plasma Kinetic energy of the ejected species	Formation of metastable structures Particulates
Secondary	Substrate temperature	Mobility of ablated species on the substrate	Formation of metastable structures
	Oxygen partial pressure	Reactive oxygen species	Oxygen content of film, Epitaxial growth Control of crystal structure
Tertiary	Substrate-target distance	Plume density near the substrate	Film Thickness

Effect of the different oxygen sources

The presence of an oxygen background during the film growth is one of the most important aspects to avoid oxygen deficient films. It has been suggested by Craciun et al. [28] that prolonged laser ablation of $La_{0.5}Sr_{0.5}CoO_3$ (LSCO) causes preferential oxygen evaporation in the target, which results in volume absorption and explosive volume boiling, causing the ejecting of droplets from the target [69]. This is not the case for the very similar LCCO compound, where even after 2×10^6 pulses to the target no changes in the film quality were observed. Gupta and Hussey [61], on the other hand, produced $YBa_2Cu_3O_{(7-x)}$ films by pulsed laser deposition in conjunction with a pulsed oxidizing source. They found, that although higher film quality could be obtained by using N_2O instead of O_2 for the gas pulse, it was still necessary to use a background of O_2 to force the equilibrium stoichiometry of the film to more complete oxidation. Our results with LCCO appear to be more consistent with the interpretation of Gupta et al.

Films grown in the O_2 background are dark and mirror like, independent of the cooling conditions. The film thickness measured by a profilometer is around 500 nm (after 42000 pulses) with a roughness in the range of 4-5 nm. The composition of the films, measured by RBS, is $La_{0.64\pm0.05}Ca_{0.35\pm0.05}Co_{0.95\pm0.05}O_{3\pm0.05}$, suggesting an almost perfectly congruent material transfer.

The effect of different oxygen sources on the oxygen content of the growth films was studied by applying only the oxygen background (8×10^{-4} mbar), or only the gas pulse (N_2O at 2 bar) or both together, during the deposition process. The compositions of the deposited films are presented in Table 2.

Table 2. Stoichiometry of the LCCO films produced with different oxygen sources.

Film	Deposition Condition	Stoichiometry
A	Gas pulse (2 bar)	$La_{0.68\pm0.05}Ca_{0.32\pm0.05}Co_{0.93\pm0.05}O_{2.6\pm0.05}$
B	Oxygen background (8×10^{-4} mbar)	$La_{0.6\pm0.05}Ca_{0.4\pm0.05}Co_{0.98\pm0.05}O_{2.75\pm0.05}$
C	Gas pulse (2 bar) + oxygen back.	$La_{0.68\pm0.05}Ca_{0.32\pm0.05}Co_{0.91\pm0.05}O_{2.91\pm0.05}$

The composition of the films changes with the different deposition conditions. When the films are grown in the presnce of 8×10^{-4} mbar of oxygen background, lower amounts of La and Ca are observed, while the best oxygen stoichiometry is obtained when the films are deposited using the gas pulse and the oxygen background. The presence of only one oxidizing source always produces films with lower oxygen content. The effect of different gases during the formation of multicomponent metal-oxides has been investigated for a long time [61, 70]. The oxygen requirements during the growth of oxides are controlled by the oxidation kinetics and the thermodynamic phase stability at the growth temperature [61]. When PLD is used as the film growing technique, a large amount of material is deposited in a very short time separated by periods with no vapor flux. This makes it necessary to have a high flux of oxygen available to oxidize the species that arrive at the substrate. In principle, the oxygen could originate exclusively from the oxide target, without the necessity of an additional oxidizing source. However, only a fraction of the oxygen is released as atoms (neutrals and ions), wile the remaining part is ejected as O_2 [71]. The adsorption probability of O_2 is less than unity due to the inefficient adsorption at the surface [72] compared to the high sticking probability of atomic O. The fact that the oxygen molecules have a lower probability of remaining at the substrate surface makes it necessary to utilize an additional oxidizing source for the effective oxidation of the cations during the film growth.

The flux of oxygen molecules is much lower in the case of the 8×10^{-4} mbar background, as compared to the flux of liberated target atoms created by laser ablation. The kinetic requirement for stoichiometric oxide growth is therefore not fulfilled (to produce an effective oxidation of the cationic species), resulting in films with an oxygen deficiency. With the synchronized N_2O gas pulse, an excess of oxygen atoms (originating from the dissociation of N_2O by collisional fragmentation by photons from the plasma, or electron-impact [70]) is created, and the species from the LCCO target arrive simultaneously at the substrate, resulting also in films with oxygen deficiency. The films with the best oxygen stoichiometry are obtained when both oxidizing sources are applied. To understand these results we have to consider not only the arrival time of the particles at the substrate, but also the time between each pulse. There exists an oxygen diffusion equilibrium that influences the oxygen content of the growing film [73, 74]. This equilibrium is partially shifted due to loss of oxygen from the film, when only the background is present ($8x10^{-4}$ mbar of oxygen). In the case of the N_2O pulse only, there is more reactive oxygen present leading to the desired oxygen partial pressure during the arrival of the atoms at the substrate. The low background of 2×10^{-6} mbar and the absence of additional oxygen between the pulses will shift the diffusion

equilibrium even further in the direction of "out diffusion". When both the N_2O pulse and the additional oxygen background are applied, a large number of oxygen atoms will arrive together with the species originated from the target at the substrate. There is now more oxygen available between the pulses, which minimizes the loss of the volatile oxygen from the surface. Therefore the films with the highest oxygen content are obtained when a gas pulse and background pressure are applied.

Fig. 5 shows the XRD patterns of LCCO films grown with different oxidizing sources. In all cases only the formation of a crystalline LCCO phase is observed, but the orientation depends on the oxidizing source.
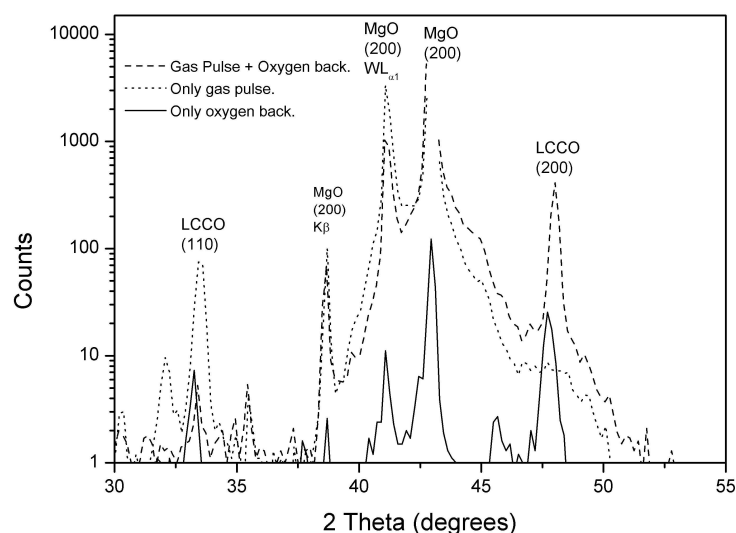

Fig. 5. XRD patterns of LCCO films grown with different oxygen sources.

An intense LCCO(200) reflex at 47.97° and a weak LCCO(110) reflex at $33.18°$ are observed for those films which were deposited using the gas pulse and the oxygen background. For those films deposited with only the oxygen background, two reflexes (200) and (110) with nearly equal intensity, whereas films deposited using the gas pulse only reveal nearly an exclusive orientation in the (110) plane. This data strongly suggest that the phase structure and preferential orientation, i.e. from (200) to (110), depends on the applied oxidizing source. The origin of this behaviour is not clear and should be the subject of further studies.

Effect of the gas pulse on the film morphology of perovskites

The surface morphology was initially studied as a function of the oxygen source, i.e. with the gas pulse alone, only with a background gas, and with the combination of both. The results are presented in Fig. 6 A, B, and C respectively.
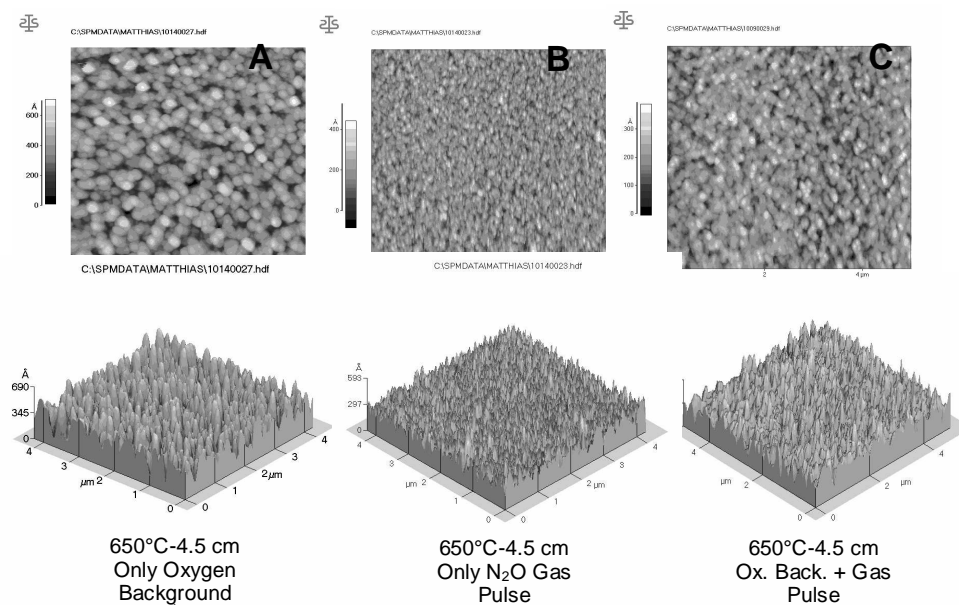
217

Fig. 6. AFM images of LCCO films deposited A: only with the oxygen background (zone T), B: only with the N_2O gas pulse (zone I) and C: with oxygen background and gas pulse (PRCLA; zone I with some zone T features,) (note the different height scales).

When the films are deposited only in the presence of the oxygen background (8×10^{-4} mbar) a combination between large (25 nm) and small columns (5.7 nm) is observed, where each column is formed by a single grain (confirmed by TEM). The roughness (≈ 7 nm) of these films obtained from the AFM images is in agreement with the values obtained by the profilometer. For films deposited only with the N_2O gas pulse (2 bar), smaller grains than in the case of the films obtained by the O_2 background are observed. The average grain size is approximately 17 nm and the roughness of the films is around 6 nm. A lower density of grains with an average size of ≈ 40 nm and a roughness of ≈ 11 nm is detected when the films are deposited with the combination of both oxygen sources, i.e. PRCLA.

The different morphologies for the different conditions can be explained by the "microstructure zones model" of Thornton [75] and its application to PLD [76]. Briefly, the model describes three different types of microstructures and relates the creation mainly to the background pressure, i.e. the kinetic energy and variation of the angle of incidence of the particles on the substrate. The different microstructures are described as:

1) Zone II structures, which are very dense structures with a very low roughness. These structures are formed at very low background pressures and with a very small target-substrate distance, i.e. the substrate is placed clearly inside the plume (the importance of the excited state species is not described in detail). These structures are not observed in our conditions.

218

2) Zone T morphology, where large scattered structures are surrounded by smaller structures. These structures are observed for conditions as in 1, but larger target-substrate distances, or at slightly higher pressures.

3) Zone I columnar structures, where a fine fibrous morphology with voids is observed (smaller structures than for zone T). These structures are formed at higher pressures with a large amount of collisions of the particles, which results in a large variation of the incidence angles of the particles arriving on the substrate.

The background pressure of the oxygen (only O_2 background) is so small that almost no collisions occur between the ablated species and the O_2 gas. The ablated particles retain their kinetic energy from the target to the substrate and arrive with a narrow angle of incidence distribution. The resulting films are dense and grow with a bimodal distribution of grain sizes, i.e. large scattered grains surrounded by small grains (*zone T*). Collisions between the ablated material and the gas pulse molecules are important and can be observed by an increase of the plasma emission when the gas pulse is applied with or without the background pressure. The ablated particles arrive at the substrate with a large variety of incidence angles and are partially thermalized before reaching the surface. This induces according to Thornton a "*self shadowing*" effect [70], resulting in the above described *zone I columnar microstructures*. Films grown with the PRCLA method reveal microstructures similar to the *zone I structures*, but with additional *zone T* features. The reason for this intermediate behavior is not yet clear, but may be a specific feature for the combination of a "high pressure zone" (gas pulse) in a low pressure background.

The previously described models explain the formation of the microstructures mainly for a fixed substrate temperature which is low compared to the melting point of the deposited material. The change from the *zone T* (low pressure) to the *columnar zone I* microstructures is mainly related to the pressure and thus the number of collisions. The larger number of collisions with higher pressures (e.g. the 'local' high pressure with the gas pulse) decreases the kinetic energy of the particles and increases the possible angles of incidence of the particles arriving at the surface.

Influence of the substrate temperature – Distance between target-substrate

Substrate temperature not only determines the initial growth of a film, but its subsequent growing as well, and therefore determining its microstructure. In general, the best value of substrate temperature corresponds to the regime where there is sufficient surface diffusion to allow surface atoms to minimize their surface energy to reach thermodynamically stable sites.

The velocity and the kinetic energy of selected neutral and charged ablation species produced by PRCLA are compiled in Table 3. The data are obtained from time- and space-resolved emission spectroscopy (not shown here).

Table 3. Velocity and calculated kinetic energy for different atoms of LCCO at the position of the substrate (4.5 cm).

Atoms	Velocity close to the substrate (km/s)	Kinetic energy (eV)
Ca I	0.19	0.74
Ca II	0.20	0.83
Co I	0.15	0.68
Co II	0.26	1.99
La II	0.16	1.92

The low kinetic energy of these species arriving at the substrate compared to PLD [77] is due to the large number of collisions with the gas pulse molecules, which occur in the initial interaction zone (around 10 times more collisions than for PLD) [78]. After the interaction zone the particles propagate freely in the direction of the substrate with almost no collisions with the oxygen molecules of the background gas (8×10^{-4} mbar). The analysis of time and space resolved emission spectra reveal several pronounced differences of PRCLA compared to PLD. First, lower kinetic energies are observed for the species arriving at the substrate. Second, a larger amount of excited states species and (excited) ionic species arrive at the substrate.

It is of course important, that the film composition will not change, if the other deposition parameters are varied to optimize/analyze the film growth. The stoichiometric index (number of atoms of a species per formula unit) of the LCCO films, as a function of the substrate temperature (at a distance of 4.5 cm) and the target-to-substrate distance (at fixed substrate temperature of 650 °C), are shown in Fig. 7A and B.
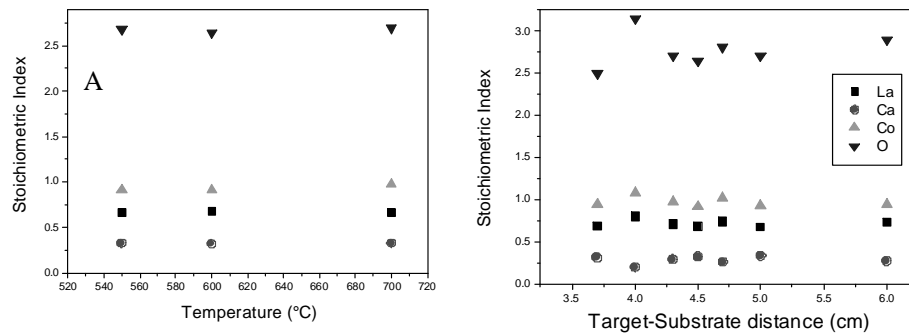

Fig. 7. Stoichiometric index for $La_{0.6}Ca_{0.4}CoO_{3-\delta}$ films A: at a target-substrate distance of 4.5 cm and B: at 650 °C.

A distance between substrate-target of 4.5 cm and a substrate temperature of 650 °C were chosen because epitaxial films could be obtained for these conditions. The results reveal that varying deposition parameters, (i.e. temperature and distance) do not affect the composition of the films, suggesting that the deposition condition can be varied over a wide range without changing the

chemical composition of the films. These results can be explained by the fact that the kinetic energy of the ablated species arriving at the substrate (0.74 to 1.99 eV), is too small to cause re-sputtering (typically observed for kinetic energies of »10 eV) of the elements from the growing film [79]. No changes in the stoichiometry are also observed when the distance is kept constant (4.5 cm) and the temperature is varied from 550 °C to 700 °C. This suggests that there is no pronounced re-evaporation of the elements from the growing films at these temperatures.

The crystallographic orientations of the grown films as a function of target-substrate distance and substrate temperature are shown in Fig. 8.
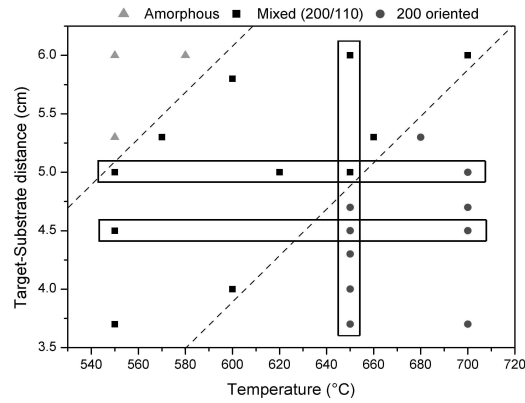

Fig. 8. Structure type of LCCO thin film deposited under various conditions of target – to - substrate distance and substrate temperature.

For a given temperature (e.g. 650 °C) and a variable target-substrate distance the films are only oriented in the (100) direction (same as the substrate) for distances up to approximately 4.7 cm; while for larger distances a mixture of (100/110) orientations is observed. A change in the orientation is also observed when the distance is kept at 4.5 cm and the temperature is increased from 550 to 700 °C. At lower temperatures a mixture of the (100/110) orientation is observed, while at higher temperatures only the (100) orientation is present. Amorphous films can be obtained at low temperatures and large distances. This control of crystallinity can be explained by the kinetic energy of the arriving particles at the substrate surface. Two energy sources are important during PLD film growth, i.e. the kinetic energy of the arriving particles and the substrate temperature, and influence therefore the crystallographic structure and film morphology. The substrate temperature is determining the crystallographic orientation when the distance (kinetic energy) is kept constant. An increase of the temperature improves the surface mobility of the clusters and atoms arriving at the substrate. In this case the number of defects is minimized (due to the surface mobility) and the film growth in the orientation of the substrate. The transition temperature from mixed orientation to epitaxial film growth is observed at higher temperatures when the target-substrate distance is increased (to e.g. 5 cm), yielding lower kinetic energies

of the arriving species. This behaviour, i.e. the synergetic effect of the energy from substrate temperature and kinetic energy, is confirmed by the corresponding experiments where the temperature is kept constant while the distance is varied. The transition of mixed orientation to single crystalline is now observed when the distances are decreased. The variation of these two parameter (distance and temperature), gives the unique opportunity to prepare films with crystallographic features that vary from amorphous to epitaxial without changing the pressure of the background gas or the substrate.

The morphology of the LCCO films grown by PRCLA were also studied as a function of temperature and target-to-substrate distance under the deposition conditions which are typical for the growth of well-defined LCCO films. The results are summarized in Table 4.

Table 4. Grain size and roughness as a function of substrate temperature and substrate-to-target distance.

Substrate temperature (°C)	Target-to-substrate distance (cm)	Average grain dimensions (nm)	Roughness rms (Å)	h distribution (Å)
650	3.7	250×8	40	150
650	4.5	262×12	53	250
650	6.0	165×11	43	160
550	4.5	141×7	29	95
650	4.5	262×12	53	250
700	4.5	237×24	99	380

The grain dimensions and roughness increase with increasing temperatures for films grown at a fixed target-to-substrate distance of 4.5 cm. An increase of the substrate temperature increases the surface mobility of clusters at the surface, resulting in the coalescence of cluster to form larger clusters that are continuing to grow with the continuing arriving species. For a fixed temperature, i.e. 650 °C, and various distances no clear tendency can be observed. An initial increase of the grain size and roughness with increasing distance is observed, which is followed by a decrease of both. The description of the microstructures of the films deposited by PRCLA according to Thornton's model is quite complicated. In most cases the film morphology can be described as a mixture between zone T and zone I features.

Fig. 9 presents the AFM pictures for films grown at different temperatures and fixed distances (3.7 and 5.0 cm). Several general trends can be observed, i.e. with increasing temperatures an increase of the size (height) of the microstructures is observed, as explained above, while for larger distances smaller features are detected, which is most pronounced at the lower temperatures.
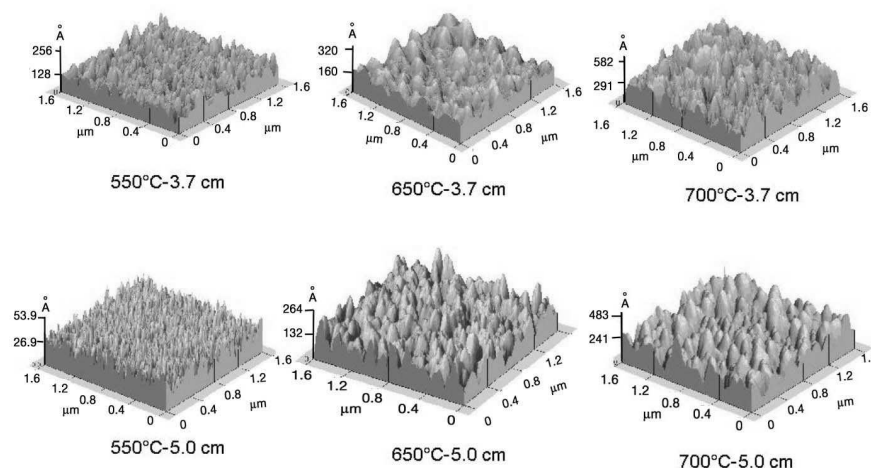
*Fig. 9. AFM images of LCCO films deposited at different temperatures
and target-substrate distances (note the different height scales).*

The changes of the structural dimensions can be explained by the higher mobility of the arriving particles and clusters due to the higher energy (either kinetic or thermal from the substrate). The description of the structures according to Thornton's model is more complicated, as all resemble the above described mixture between zone T and zone I, with the possible exception of the film grown at 550 °C at a distance of 5.0 cm. The morphology of this film can probably be described as a zone I structure. This suggests that in principle zone I structures are obtained by PRCLA, but only at low temperatures and kinetic energies. Another possible parameter that must be considered is the energy of the excited state species in the plasma. Optical observation of the plasma during PRCLA suggests that the plasma extends much further from target and is much brighter than in the case of normal PLD. It is therefore quite probable that a pronounced amount of excited states species will also arrive at the substrate, thus adding to the energy balance of the growing film.

Electrochemical characterization

Gas diffusion vs. thin films of $La_xCa_{1-x}CoO_3$

The comparison between the gas diffusion and the thin films will be considered in this paragraph just in a qualitative way. An electrochemical process involves several steps, i.e. mass transfer, chemical reaction, adsorption/desorption, and electron transfer. The mass transfer of oxygen from the solution to the electrode surface is assumed to be the same for both electrode types. For the last two steps a pronounced difference exists between the gas diffusion and the thin film electrodes. In the gas diffusion electrode the surface is porous and the real area of the electrode is extremely difficult to determine. Additionally, the reactive area consists of carbon and catalyst. Contrary to this, the thin film electrode consists of

223

a compact structure with very few small pores. The surface area can be assumed to have a similar value as the geometrical area and only the catalyst is present on the surface. These differences suggest that different adsorption mechanisms are present on both surfaces. If we consider the electron transfer as well, the situation becomes even more complicated due to the fact that for thin films the electron transfer will be possible only through electron holes or oxygen vacancies and determination of their presence in the crystal lattice during the redox-reaction is nearly impossible. For the gas diffusion electrode the electron transfer will take place on different surfaces, i.e. on the perovskite (oxygen evolution) and on the carbon followed by the perovskite (oxygen reduction). Any attempt at a quantitative comparison between the systems will therefore be associated with a large systematic error.

Polarization curves under steady state conditions were measured to study the electrochemical activity of the LCCO materials, i.e. gas diffusion and thin film electrodes. For these measurements two electrodes were selected: the optimized gas diffusion electrode was chosen as a reference to be compared with our model system, and a LCCO single crystalline film deposited on MgO(100). The results are presented in Fig. 10.
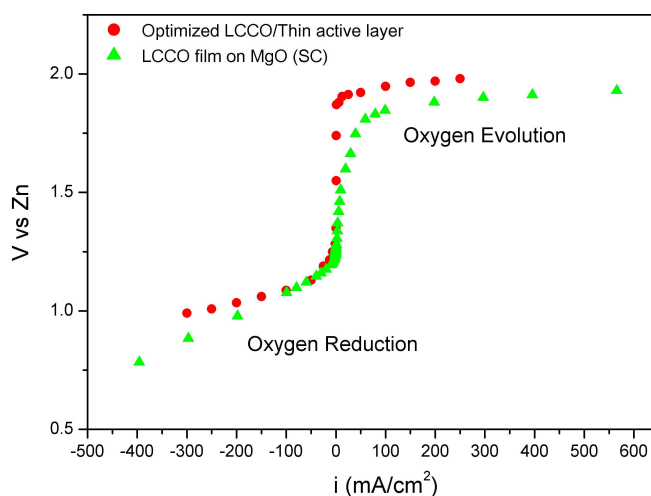

Fig. 10. Polarization curves of an LCCO gas diffusion electrode and LCCO thin films deposited on MgO (single crystalline) for the oxygen reactions.

The polarization curves show that the model systems present a slightly smaller overpotential for the two oxygen reactions than the optimized gas diffusion electrode. The model system is more active for the oxygen evolution reaction while the gas diffusion electrode is more active for the oxygen reduction reaction. An important factor is that current density values are comparable to the ones obtained for the carbon-based perovskite gas diffusion electrodes, indicating that thin films can be used as model system to screen different perovskite electrodes.

Effect of the crystallinity

Most of the reported electrochemistry with solid electrodes involves polycrystalline materials. Such electrodes consist of a variety of small domains with different crystal faces and edges which will face the electrolyte. Different crystal faces exhibit different properties (e.g. work function) so that the behavior observed at a polycrystalline electrode represents an average of that for a number of different crystal planes and sites. One possible way to analyze solid electrode interfaces and their influence in a specific reaction can be performed by using single-crystal electrodes. The most common metals used as electrodes, i.e. Pt, Pd, Ag, Ni and Cu, form face-centered cubic crystal structures.

Three low index faces (100), (110), and (111) are the surfaces most frequently used as electrodes, because they tend to be stable and can be polished to yield fairly smooth, uniform surfaces. Nevertheless, even the most carefully prepared surfaces are not atomically smooth over areas larger than a few square micrometers, and they inevitably show steps, edges, and defect sites.

Catalytic and adsorptive properties of solid surfaces can depend upon the crystal face. An example is the difference in cyclic voltammograms for the adsorption/desorption of hydrogen on the different surfaces of platinum [80].

The importance of the crystallinity on several electrochemical reactions and the fact that until now the studies for the oxygen evolution/reduction on LCCO were only performed on polycrystalline gas diffusion electrodes were one of the driving forces to perform experiments using thin LCCO films with different crystallographic orientations. Only for dense films will the observed catalytic activity correspond to the catalyst and the active area of the electrode can be easily determined and compared to other electrodes.

The polarization curves for thin amorphous, mixed, and single crystalline LCCO films are compared in Fig. 11.
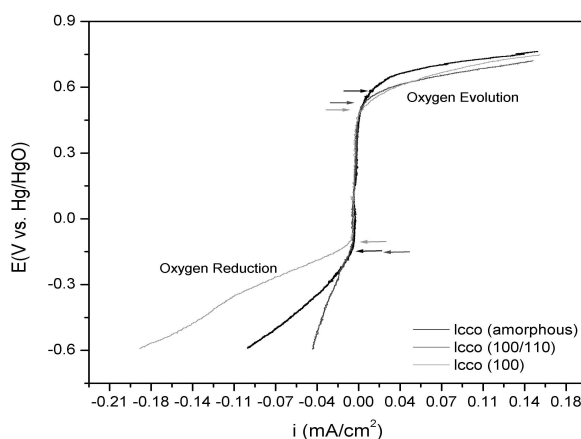

Fig. 11. Polarization curves of amorphous, single- and polycrystalline
LCCO thin films deposited on MgO(100) substrates.

The polarization curves show that the crystallinity influences directly the catalytic activity for oxygen reduction and evolution reactions (measured by the

overpotential). The overpotential is the difference between the values indicated with the arrows in Fig. 16. The film with the smallest overpotential (597 mV) is the (100) oriented sample followed by the film with mixed 110 and 200 orientation (679 mV) and the amorphous film (738 mV). An electrochemical process, as discussed previously, involves several steps, i.e. mass transfer, chemical reaction, adsorption/desorption, and electron transfer. The result indicates that the only step that can influence the electrochemical behaviour of these three electrodes, i.e. the adsorption of the oxygen molecules, is affected by the surface energy of the electrode surface, which depends on the exposed crystallographic orientation and grain boundaries. It can also be concluded that the phase with (100) orientation presents the best performance.

In the last part of this preliminary study we deposited LCCO films on MgO substrates with different orientations (e.g. (100), (110), and (111)) under the standard deposition conditions. Prior to electrochemical measurements the film were measured to determine their stoichiometry and crystallographic orientations. The stoichiometry of LCCO films deposited on different MgO substrates is presented in Table 5.

Table 5. Composition of LCCO thin films, deposited on different orientations of MgO substrates.

Film Name	Stoichiometry (ratio La:Ca:Co:O)
LCCO, MgO(100)	$La_{0.68\pm0.05}Ca_{0.32\pm0.05}Co_{0.93\pm0.05}O_{2.75\pm0.05}$
LCCO, MgO(110)	$La_{0.65\pm0.05}Ca_{0.35\pm0.05}Co_{0.94\pm0.05}O_{2.75\pm0.05}$
LCCO, MgO(111)	$La_{0.68\pm0.05}Ca_{0.32\pm0.05}Co_{0.97\pm0.05}O_{2.7\pm0.05}$

The results presented in Table 5 show that the films are almost identical in their composition, confirming that the electrochemical performance will correspond just to the LCCO compound.

From the XRD diffractograms presented in Fig. 12, it is possible to conclude that the main problem when MgO(110) and (111) are used, that it is not possible to obtain epitaxial growth of the perovskite phase in the (110) and (111) orientation. Nevertheless, the obtained films were measured.
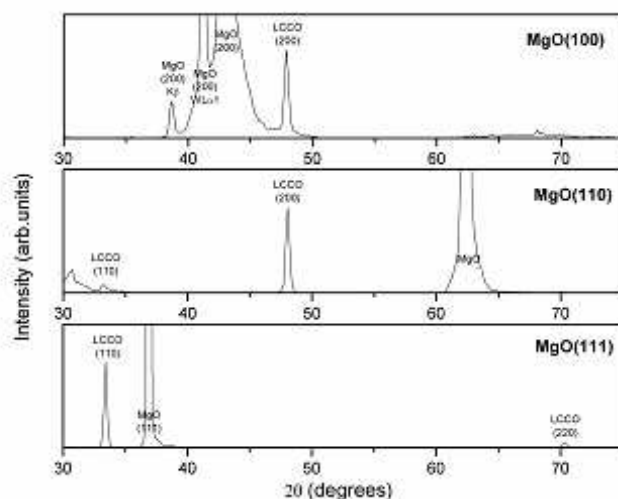
Fig. 12. X-ray diffractogram of a LCCO films deposited on MgO(100),
(110), and (111).

The film deposited on MgO(100) shows only the (200) reflection, indicating that the film grows epitaxially to the substrate. The film deposited on MgO(110) present a preferential orientation in the (100) direction with a small peak due to the (110) reflexion at 33.3°. The film deposited on MgO(111) is preferential oriented in the (110) direction. The results indicate that the grown film is adopting mainly the orientation with preferable energy and lattice match. For the films grown on MgO(110) and (111) a weak reflexion is observed in the substrate orientation. This result indicates that at the initial growth stage the film assumes the substrate orientation, and then changes after a critical thickness to obtain an energetically more stable orientation. This effect has been observed previously by Kief and Egelhoff for Fe and Co [81] and by Lu et al. for LCMO [82].

Fig. 13 presents the polarization curves for LCCO films deposited on MgO(100), MgO(110) and MgO(111). The overpotential between both oxygen reactions is affected by epitaxy, crystallinity, and orientation of the films.
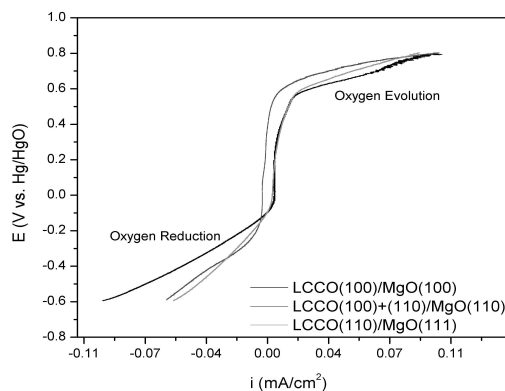

Fig. 13. Polarization curves for LCCO thin films deposited on MgO
substrates cut in different orientations.

The film with the smallest overpotential is the one grown on the MgO(100) showing an orientation in (100) direction followed by the film with mixed 110 and 100 orientation on the MgO(110) substrates and the film with preferential (110) orientation on the MgO(111) substrate. As explained above, we can assume that the adsorption of the oxygen molecules is affected by the surface energy of the electrode surface, which depends on the exposed crystallographic orientation and grain boundaries. The result indicates that in the case of the $La_{0.7}Ca_{0.3}CoO_3$ electrodes the best performance is obtained for the (100) orientation, which should have the lowest surface energy.

Substitution of Co by Mn in the $La_{0.7}Ca_{0.3}CoO_3$ perovskite

Another parameter that can improve the catalytic activity of the perovskite is a change of the composition (from Co to Mn) or an additional substitution (Ni into Mn). We tested these possibilities by preparing these types of films. The film stoichiometry of LCCO, LCMO, and LCMNO was measured by RBS and the results are summarized in Table 6.

Table 6. Composition of different perovskite oxides thin films, deposited on MgO(100).

Film Name	Stoichiometry
LCCO	$La_{0.68}Ca_{0.32}Co_{0.93}O_{2.75}$
LCMO	$La_{0.71}Ca_{0.29}Mn_{0.9}O_{2.8}$
LCMNO	$La_{0.71}Ca_{0.29}Mn_{0.82}Ni_{0.1}O_{2.8}$

The film composition indicates that the ablation is congruent for LCCO whereas a small loss of Mn ions is observed for LCMO [83]. It has been suggested by Choi et al. [84], that the structural difference and lattice mismatch between LCMO and MgO, induce dislocation of Mn ions along grain boundaries, facilitating the loss of Mn ions during oxygen annealing. Boyd et al. [83] have also observed loss of Mn when the substrate temperature is higher than 700 °C. In our case the observed results can be explained mainly due to Mn loses during the cooling procedure in air where the oxygen pressure is quite high.

The comparison between the gas diffusion and the thin films will be considered again just in a qualitative way. In order to observe the differences in the substitution of Co by Mn, the polarization curves of LCMO and LCMNO materials are plotted together with the data from LCCO. Carbon-based electrodes of LCCO, LCMO and LCMNO (left) were produced as reference to be compared with the thin film model systems (right) and are shown in Fig. 14.
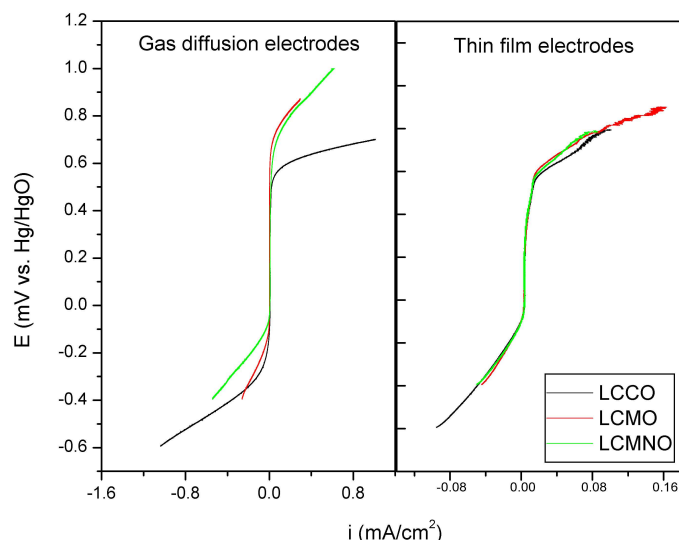
Fig. 14. Polarization curves for LCCO, LCMO, and LCMNO gas diffusion and thin film electrodes deposited on MgO(100).

The polarization curves show that in general as for LCCO the thin films of LCMO and LCMNO present a slightly smaller overpotential for the two oxygen reactions than the respectively optimized carbon-based perovskite gas diffusion electrodes. An important factor is that current density values of the thin films are comparable to the ones obtained for the carbon-based perovskite gas diffusion electrodes, indicating that thin films can be used as model system to screen different perovskite electrodes. A different overpotential is observed for the three perovskite phases in the gas diffusion electrodes. The overpotential was the lowest for cobaltate containing electrodes and slightly higher but quite similar for the two manganate containing electrodes. This suggests that the LCCO electrode has a better performance than the LCMO and LCMNO electrode. In contrast, no difference in the overpotential is observed for different perovskite thin films electrodes. The comparison of the thin films electrodes has to be considered carefully due to the crystallographic differences of the electrodes. The manganate electrodes present several crystal faces with one main orientation compared to the cobaltate electrode where only one single orientation is observed. These different crystal faces exhibit different properties (i.e. work function) resulting in an electrochemical behaviour that represents an average for the number of different crystal planes present in the electrode. The observed result, i.e. that different materials behave in the same way, is not conclusive because this effect can be due to the different crystallographic quality and not exclusively due to the different materials. For this reason new studies with single crystalline manganate electrodes are planned. Another property which can influence the catalytic activity is the surface. Two aspects were analyzed to allow a more precise comparison between the different electrodes. The morphology was studied by AFM, but no significant differences in the structure and in the surface area were found, and the chemical

229

composition of the surface was studied by XPS [60] where no pronounced differences were detected. The only variation of the surface composition is the amount of adventitious carbon absorbed which is removed prior the steady state measurements by consecutive electrochemical scans. Another result is the difference of the slopes for oxygen reduction and evolution between the different materials on the gas diffusion and thin films electrodes. The different perovskite-gas diffusion electrodes show different slopes for both oxygen reactions. Nevertheless, the different thin films show no difference for the oxygen reduction and only a slight difference for the oxygen evolution reaction. This result can be explained by to the different mechanisms present for the oxygen reaction. The oxygen reduction proceeds through a sequential mechanism [85], where the oxygen is reduced on the carbon to form a peroxide, followed by the peroxide decomposition on the oxide. This can be observed for the gas diffusion electrode where probably the combination of the carbon and the perovskite activity produce different slopes, which can not be observed on the thin films electrodes where no carbon is present. For the oxygen evolution the perovskite acts directly as catalysts. This can be observed in both types of electrodes, but is more pronounced for the gas-diffusion electrode, which can be related to the real area of the electrode, which is larger for a porous structure.

Parameters influencing the deposition of Lithium Spinel films

In the case of Li-spinels different substrate materials can result in different preferred crystallographic orientation of the deposited film. Several authors [86, 87] have shown that the deposited films form a polycrystalline spinel with random orientation on substrates such as platinum, stainless steel and silicon. However, Rougier et al. have shown that the utilization of $Si(100)/Si_3N_4$ substrates yields to a preferred (111) orientation [88]. Another parameter that influences the crystallinity of the films is the substrate temperature [89-91]. At higher substrate temperatures the characteristic reflexes in the X-ray-diffraction patterns ((111) at 19.5° and (444) at ~ 45°, [91]) increases These reflexes are associated with the degree of crystallinity of the films. This influence has previously been shown by various authors [86, 89, 92, 93] who also analyzed the influence of the oxygen background pressure and target composition. Julien et al. [89] revealed that films grown from a target with an excess of 5% of lithium shows very poor crystallinity. With an increasing excess of lithium in the target (up to 15%), the deposited films reach the regular spinel crystal structure, which can also be improved with increasing substrate temperatures. These experiments where carried out at relatively low substrate temperatures, ranging from 100 °C to 300 °C and at a very low background pressure of $6.7 \cdot 10^{-5}$ mbar of O_2 and with non stoichiometric targets. The necessary experimental parameters may vary from theses values when using a stoichiometric target.

As described earlier for the perovskite-type phases, Pulsed Reactive Cross-Beam Laser Deposition (PRCLA) is in principle a very suitable method for the deposition of complex oxides. However, in the case of spinels the utilization of the PRCLA set up is not applicable due to the crossed gas pulse, which significantly increases the scattering of light atoms, such as lithium. The influence of the crossed gas pulse on the crystallographic structure and stoichiometry of the film is clearly

visible in Fig. 15, which shows the X-ray diffraction patterns of a $LiMn_2O_4$ film on a titanium foil which was deposited with the PRCLA set up.
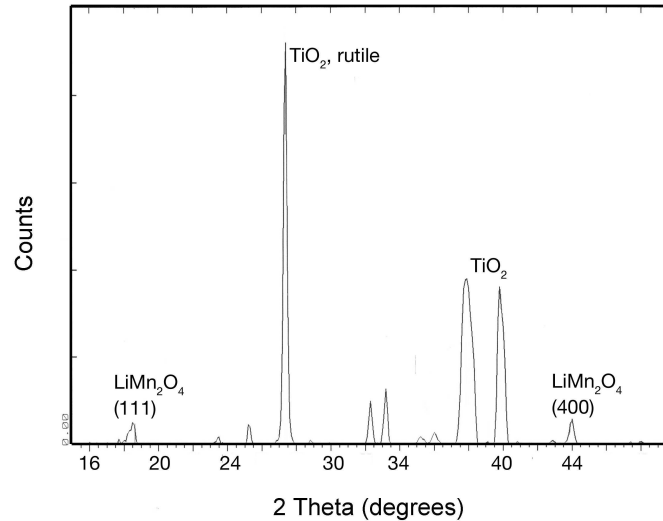

Fig. 15. X-ray diffraction patterns of a $LiMn_2O_4$ film deposited on a polished titanium foil.

The diffraction patterns shows clear evidence for the formation of a Ti-oxide layer, mostly in the rutile phase (reflexes at 27.5°, ~ 38° and ~ 40°), in addition to the very weak reflexes that can be assigned to the Li-spinel ((111) at 18.5°, (400) at ~ 44°). This TiO_2 layer must be formed in air or prior to deposition in the chamber, when the substrate is heated and oxygen is introduced to the chamber. This oxide layer is of unknown thickness and roughness which makes it very difficult, if not impossible, to determine the oxygen fraction in the $LiMn_2O_4$ film by RBS. The films obtained by this setup did not show the expected electrochemical activity.

In Fig. 16 the X-ray diffraction patterns of $LiMn_2O_4$ deposited on Si(100) using the classical PLD setup (without the gas pulse) at an oxygen pressure of 0.16 mbar and a substrate temperature of 510 °C is shown. A KrF excimer laser (248 nm) with a repetition rate of 10 Hz, a fluence of 3-4 J/cm^2 and 180'000 pulses was used for the deposition. The diffraction patterns show clearly the reflexes that can be attributed to a spinel structure of the film and is in agreement with results reported by other groups [86, 94, 95].
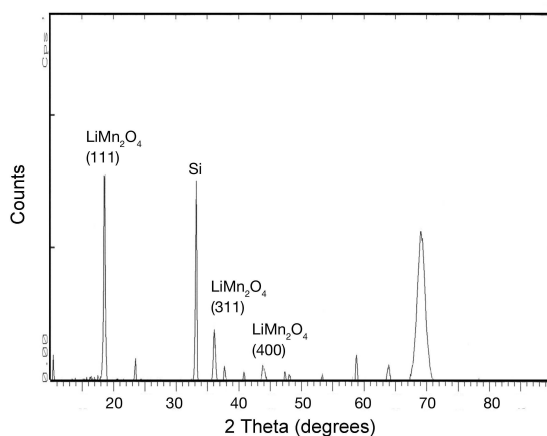
Fig. 16. X-ray diffraction patterns of a LiMn₂O₄ film deposited on Si(100).

The cyclic voltammogram of a $LiMn_2O_4$ film deposited on polished titanium foil under the same conditions is shown in Fig. 17. The intercalation of lithium into the Spinel structure can be observed between 3.5 V and 3.6 V. The typical step behavior is not pronounced for the insertion, and the extraction of Li is even less visible.
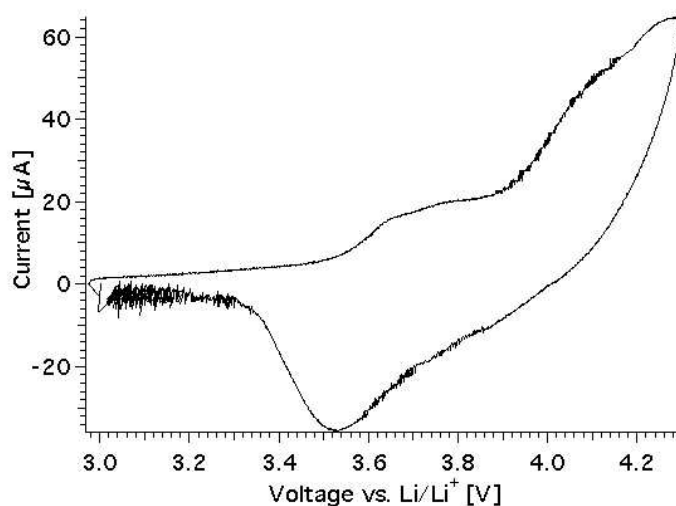

Fig. 17. Cyclic voltammogram of a 0.4 μm thick LiMn₂O₄ in
Ethylencarbonat / Dimethylcarbonat 1:1 + 1M LiPF₆

This plot resembles the cyclovoltammogram published by Chromik et al. [96] for thermally deposited $LiMn_2O_4$ film on Titanium foil. The films in this work revealed a pronounced lithium deficiency (Li/Mn ratio below 0.5), which leads to the conclusion that the films in Fig. 17 have also a pronounced lithium deficiency.

232

Nevertheless, the X-ray diffraction patterns in Fig. 6 give clear evidence for the presence of a spinel phase.

The pronounced differences in the X-ray diffraction patterns between the films deposited by PRCLA (Fig. 15) and later by PLD (Fig. 16) demonstrate the effect of the utilization of a crossed gas pulse on the crystallinity and stoichiometry of $LiMn_2O_4$ films. lithium with its low atomic mass can more easily be scattered than the other much heavier atoms, even oxygen. The gas pulse in PRCLA creates a relatively high local pressure which results in a pronounced scattering of the lithium atoms from the plasma throughout the chamber and not any more directed at the substrate. This results in lithium deficient films. There are two possible ways to overcome this problem. One possibility is to utilize an excess of lithium in the target [89, 93, 94], or to utilize the classical PLD setup (without the gas pulse). Morcrette et al. [86, 92] have shown that there is only a small window for the oxygen background pressure that can be used for the stoichiometric deposition of $LiMn_2O_4$. The group analyzed $LiMn_2O_4$ films deposited on polycrystalline platinum substrates by PLD from a stoichiometric target. The oxygen pressure was varied between 10^{-6} and 1 mbar [86] and between 0.2 and 0.4 mbar [92]. A quadrupled Nd:YAG laser with a wavelength of 266 nm, 5 Hz repetition rate and with a fluence of 2 J/cm^2 was applied for these experiments,. No post-deposition annealing was performed to eliminate the possibility of compositional changes in the film. The results indicate that a low background pressure results in lithium deficient films. This is most probably due to the low vapor pressure of Lithium oxide which could evaporate at lower oxygen background pressure and higher substrate temperatures.

The higher oxidation states of manganese, such as Mn^{3+} in $Li_xMn_2O_4$ are not formed in the film since lower oxidation states, such as Mn^{2+} are favored [86]. In Fig. 18 the RBS analysis of the Li/Mn ratio as a function of oxygen pressure and substrate temperature is shown, which reveals a manganese deficiency due to high background pressure [92].
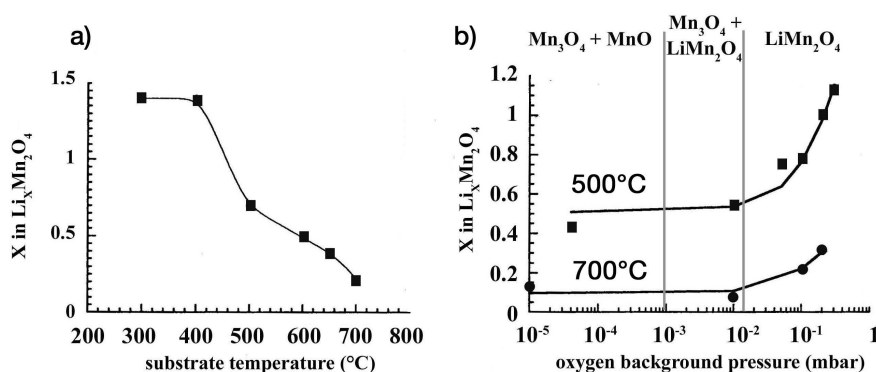

Fig. 18. (a) RBS analysis of the Li stoichiometry coefficient as a function of temperature for the pressure of 0.1 mbar. (b) RBS analysis of the Li stoichiometry coefficient as a function of the oxygen pressure for two temperatures 500 °C (top curve) and 700 °C (bottom curve). Adopted from [86].

The optimised pressure for obtaining a $LiMn_2O_4$ spinel phase is 0.2 mbar. The electrochemical characterization, i.e. cyclic voltammogram, of these films correspond to what is expected from $LiMn_2O_4$ [86, 92].

Conclusions

The application of PRCLA as deposition technique allows the preparation of thin films of perovskite-type oxide materials with a nearly completely filled oxygen sublattice and without additional processing steps (e.g. annealing). The low kinetic energy of the atoms/species arriving at the substrate surface prevents re-sputtering, which yields films with the same composition as the target material, for a variety of target-substrate distances. The crystallinity of the films can be controlled from amorphous to single crystalline, by varying the substrate temperature, the substrate and its orientation, and the distance between target and substrate. Our studies have revealed that the crystallinity has a pronounced influence on the catalytic activity. The morphology of the films can be controlled as well by selecting the deposition parameters. The morphology of the films can not be directly described with existing models, most probably due to the additional influence of parameters, e.g. plasma expansion /duration and amount of excited ionic species, which are specific to PRCLA.

The films produced by PRCLA prove the possibility to apply thin films as model systems for electrochemical studies.

Epitaxial films of LCCO reveal a higher activity than films with mixed orientation, followed by amorphous films. The crystallographic orientation of the films has also a pronounced influence on the catalytic activity. Films with (100) orientation reveal the highest catalytic activity. The influence of the crystallinity is so high, that thin films with different composition and different crystallographic structure yield by chance the same catalytic activity.

For the Li-spinels, it can be concluded that the deposition of $LiMn_2O_4$ is most practicable with a standard PLD equipment, but physical constraints such as atom scattering and vapor pressure leave only a small window for the optimum experimental parameters.

Acknowledgements

References

[1] T. Watanabe, A. Nakajima, R. Wang, M. Minabe, S. Koizumi, A. Fujishima, K. Hashimoto, Thin Solid Films **351**(1-2), 260-263 (1999).

[2] J. G. Bednorz, K. A. Muller, Zeitschrift Für Physik B-Condensed Matter, **64**(2), 189-193 (1986).

[3] F. S. Galasso, Structure Properties and Preparation of Perovskite-type Compounds. 1969, London: Pergamon Press.

[4] C. D. Chandler, C. Roger, M. J. Hampdensmith, Chemical Reviews **93**(3), 1205-1241 (1993).

[5] A. F. Wells, Structural Inorganic Chemistry. 1986, Oxford: Clarendon Press.

[6] L. G. Tejuca, J. L. G. Fierro, J. M. D. Tascon, Advances in Catalysis, ed. D.D. Eley, H. Pines, P. B. Weisz. 1989, New York: Academic Press.

[7] H. Song, W. Kim, S. J. Kwon, J. Kang, Journal of Applied Physics **89**(6), 3398-3402 (2001).

[8] J. T. Cheung, P. E. D. Morgan, D. H. Lowndes, X. Y. Zheng, J. Breen, Structural And Electrical-Properties Of La0.5Sr0.5CoO3 Epitaxial-Films. Applied Physics Letters **62**(17), 2045-2047 (1993).

[9] S. Müller, F. Holzer, O. Haas, Journal of Applied Electrochemistry **28**(9), 895-898 (1998).

[10] B. D. McNicol, A. A. J. Rand, eds. Power Sources for Electric Vehicles. 1984, Elsevier: Amsterdam.

[11] I. Buchmann, Batteries in a portable world. 2001, Richmond: Cadex Electronics.

[12] C. Fierro, R. E. Carbonio, D. Scherson, E. B. Yeager, Insitu Mossbauer-Effect Spectroscopy of A Model Iron Perovskite Electrocatalyst. Electrochimica Acta **33**(7), 941-945 (1988).

[13] A. Weidenkaff, S. G. Ebbinghaus, T. Lippert, Chemistry of Materials **14**(4), 1797-1805 (2002).

[14] P. N. Ross, M. Sattler, The Corrosion Of Carbon-Black Anodes In Alkaline Electrolyte. 3. The Effect of Graphitization On The Corrosion-Resistance of Furnace Blacks. Journal of The Electrochemical Society **135**(6), 1464-1470 (1988).

[15] J. Prakash, D. Tryk, E. Yeager, Journal of Power Sources **29**(3-4), 413-422 (1990).

[16] J. Prakash, D. Tryl, W. Aldred, E. Yeager, Electrochemistry in Transition, ed. O. J. Murphy, S. Srinivasan, and B. E. Conway. 1992, New York: Plenum Press.

[17] Y. F. Yang, Y. H. Zhou, Journal of Electroanalytical Chemistry **397**(1-2), 271-278 (1995).

[18] A. M. Kannan, A. K. Shukla, S. Sathyanarayana, Journal of Power Sources **25**(2), 141-150 (1989).

[19] J. O. Bockris, T. Otagawa, Journal of The Electrochemical Society **131**(2), 290-302 (1984).

[20] S. Müller, K. Striebel, O. Haas, Electrochimica Acta **39**(11-12), 1661-1668 (1994).

[21] M. Tsionsky, O. Lev, Journal of The Electrochemical Society **142**(7), 2132-2138 (1995).

[22] C. Fischer, N. Alonsovante, S. Fiechter, H. Tributsch, Journal of Applied Electrochemistry **25**(11), 1004-1008 (1995).

[23] R. E. Carbonio, C. Fierro, D. Tryk, D. Scherson, E. Yeager, Journal of Power Sources **22**(3-4), 387-398 (1988).

[24] R. N. Singh, N. K. Singh, J. P. Singh, Electrochimica Acta **47**(24), 3873-3879 (2002).

[25] T. Horita, K. Yamaji, N. Sakai, H. Yokokawa, A. Weber, E. Ivers-Tiffee, Electrochimica Acta **46**(12), 1837-1845 (2001).

[26] H. Tamara, H. Yoneyama, Y. Matsumoto, Electrodes of Conductive Metallic Oxides, ed. S. Trasatti. 1980, New York: Elsevier.

[27] A. K. Shukla, C. L. Jackson, K. Scott, The promise of fuel cell-based automobiles. Bulletin of Materials Science **26**(2), 207-214 (2003).

[28] G. P. Luo, Y. S. Wang, S. Y. Chen, A. K. Heilman, C. L. Chen, C. W. Chu, Y. Liou, N. B. Ming, Applied Physics Letters **76**(14), 1908-1910 (2000).

[29] N. L. Wu, W. R. Liu, S. J. Su, Electrochimica Acta **48**(11), 1567-1571 (2003).

[30] J. B. Goodenough, R. Manoharan, Electrochimical Society Proceedings, **92**(11), 1992.

[31] K. Kinoshita, Electrochemical Oxygen Technology. 1992, New York: John Wiley & Sons.

[32] J. B. Goodenough, A. Manthiram, A. C. W. James, Material Research Society Symposium Proceedings **135,** 391 (1989).

[33] D. W. Murphy, R. J. Cava, S. M. Zahurak, A. Santoro, Ternary LixTiO2 Phases From Insertion Reactions. Solid State Ionics **9-10**(DEC), 413-417 (1983).

[34] L. A. Depicciotto, M. M. Thackeray, Materials Research Bulletin **20**(2), 187-195 (1985).

[35] L. A. Depicciotto, M. M. Thackeray, Lithium Insertion Extraction Reactions With $LiVO_2$ And LiV_2O_4. Solid State Ionics **18-9,** 773-777 (1986).

[36] G. Pistoia, M. Pasquali, L. A. Depicciotto, M. M. Thackeray, Solid State Ionics **28**, 879-885 (1988).

[37] M. M. Thackeray, W. I. F. David, P. G. Bruce, J. B. Goodenough, Lithium Insertion Into Manganese Spinels. Materials Research Bulletin **18**(4), 461-472 (1983).

[38] M. H. Rossouw, A. Dekock, L. A. Depicciotto, M. M. Thackeray, Materials Research Bulletin **25**(2), 173-182 (1990).

[39] F. Lubin, A. Lecerf, M. Broussely, J. Labat, Journal of Power Sources **34**(2), 161-173 (1991).

[40] K. M. Colbow, J. R. Dahn, R. R. Haering, Journal of Power Sources **26**(3-4), 397-402 (1989).

[41] L. A. Depicciotto, M. M. Thackeray, Materials Research Bulletin **21**(5), 583-592 (1986).

[42] M. Wakihara, O. Yamanoto, Lithium Ion Batteries. 1998, New York: Wiley-VCH.

[43] K. A. Striebel, A. Rougier, C. R. Horne, R. P. Reade, E. J. Cairns, Journal of the Electrochemical Society **146**(12), 4339-4347 (1999).

[44] H. S. Wang, D. Eissler, Y. Kershaw, W. Dietsche, A. Fischer, K. Ploog, D. Brunner, Applied Physics Letters **60**(6), 778-780 (1992).

[45] C. Dubourdieu, M. Rosina, H. Roussel, F. Weiss, J. P. Senateur, J. L. Hodeau, Applied Physics Letters **79**(9), 1246-1248 (2001).

[46] T. G. S. Cruz, M. U. Kleinke, A. Gorenstein, Applied Physics Letters **81**(26), 4922-4924 (2002).

[47] V. G. Prokhorov, Y. P. Lee, K. W. Kim, V. M. Ishchuk, I. N. Chukanova, Applied Physics Letters **80**(13), 2353-2355 (2002).

[48] F. J. Cadieu, L. Chen, B. Li, T. Theodoropoulos, Journal of Applied Physics **87**(9), 6770-6772 (2000).

[49] R. Rauer, J. Backstrom, D. Budelmann, M. Kurfiss, M. Schilling, M. Rubhausen, T. Walter, K. Dorr, S. L. Cooper, Applied Physics Letters **81**(20), 3777-3779 (2002).

[50] Pulsed Laser Deposition of Thin Films, ed. D. B. Chrisey and G. K. Hubler. 1994, New York: John Wiley & Son.

[51] P. R. Willmott, J. R. Huber, Reviews of Modern Physics **72**(1), 315-328 (2000).

[52] D. Bäuerle, Laser Processing and Chemistry. 2000, Berlin: Springer Verlag.

[53] T. Kobayashi, H. Akiyoshi, M. Tachiki, Applied Surface Science **197**, 294-303 (2002).

[54] A. Giardini, V. Marotta, A. Morone, S. Orlando, G. P. Parisi, Applied Surface Science **197**, 338-342 (2002).

[55] C. Vivien, M. Dinescu, P. Meheust, C. Boulmer-Leborgne, A. P. Caricato, J. Perriere, Applied Surface Science **129**, 668-673 (1998).

[56] A. Narazaki, T. Sato, Y. Kawaguchi, H. Niino, A. Yabe, T. Sasaki, N. Koshizaki, Applied Surface Science **197**, 438-441 (2002).

[57] V. Craciun, D. Craciun, Z. Chen, J. Hwang, R. K. Singh, Applied Surface Science **168**(1-4), 118-122 (2000).

[58] J. W. Yoon, T. Sasaki, N. Koshizaki, Applied Physics A-Materials Science & Processing **76**(4), 641-643 (2003).

[59] G. Radhakrishnan, P. M. Adams, Applied Physics A-Materials Science & Processing **69**, S33-S38 (1999).

[60] M. J. Montenegro, M. Dobeli, T. Lippert, S. Muller, B. Schnyder, A. Weidenkaff, P. R. Willmott, A. Wokaun, Physical Chemistry Chemical Physics **4**(12), 2799-2805 (2002).

[61] A. Gupta, B. W. Hussey, Applied Physics Letters **58**(11), 1211-1213 (1991).

[62] P. R. Willmott, F. Antoni, Applied Physics Letters **73**(10), 1394-1396 (1998).

[63] M. J. Montenegro, J. Lippert, S. Muller, A. Weidenkaff, P. R. Willmott, A. Wokaun, Applied Surface Science **197**, 505-511 (2002).

[64] S. Müller, F. Holzer, O. Haas, C. Schlatter, C. Comninellis, Chimia **49**(1-2), 27-32 (1995).

[65] S. Müller, O. Haas, C. Schlatter, C. Comninellis, Journal of Applied Electrochemistry **28**(3), 305-310 (1998).

[66] F. J. Morin, J. P. Maita, Physical Review **96**(1), 28-35 (1954).

[67] L. R. Doolittle, Nuclear Instruments & Methods In Physics Research Section B-Beam Interactions With Materials And Atoms **15**(1-6), 227-231 (1986).

[68] H. Arai, S. Muller, O. Haas, Journal of The Electrochemical Society **147**(10), 3584-3591 (2000).

[69] V. Craciun, D. Craciun, J. Perriere, I. W. Boyd, Journal of Applied Physics, **85**(6), 3310-3313 (1999).

[70] A. Gupta, B. W. Hussey, M. Y. Chern, Physica C **200**(3-4), 263-270 (1992).

[71] C. H. Chen, R. C. Phillips, M. P. McCann, Physical Review B, **39**(4), 2744-2747 (1989).

[72] J. R. Engstrom, T. Engel, Physical Review B, **41**(2), 1038-1041 (1990).

[73] M. Cherry, M. S. Islam, C. R. A. Catlow, Journal of Solid State Chemistry **118**(1), 125-132 (1995).

[74] Y. M. L. Yang, A. J. Jacobson, C. L. Chen, G. P. Luo, K. D. Ross, C. W. Chu, Applied Physics Letters **79**(6), 776-778 (2001).

[75] J. A. Thornton, Journal of Vacuum Science & Technology A-Vacuum Surfaces And Films **4**(6), 3059-3065 (1986).

[76] M. Koubaa, A. M. Haghiri-Gosnet, R. Desfeux, P. Lecoeur, W. Prellier, B. Mercey, Journal of Applied Physics **93**(9), 5227-5235 (2003).

[77] H. J. Dang, Q. Z. Qin, Chemical Physics Letters **354**(3-4), 210-216 (2002).

[78] M. J. Montenegro, C. Clerc, T. Lippert, S. Muller, P. R. Willmott, A. Weidenkaff, A. Wokaun, Applied Surface Science **208**, 45-51 (2003).

[79] T. Scharf, H. U. Krebs, Applied Physics A-Materials Science & Processing **75**(5), 551-554 (2002).

[80] J. A. Bard, L. R. Faulkner, Electrochemical Methods. 2000, New York: John Wiley & Sons.

[81] M. T. Kief, W. F. Egelhoff, Physical Review B, **47**(16), 10785-10814 (1993).

[82] C. J. Lu, Z. L. Wang, C. Kwon, Q. X. Jia, Journal of Applied Physics,. **88**(7), 4032-4043 (2000).

[83] I. W. Boyd, W. Zhang, Applied Surface Science **129**, 410-417 (1998).

[84] H. S. Choi, W. S. Kim, B. C. Nam, H. Hur, Applied Physics Letters **78**(3), 353-355 (2001).

[85] Y. Shimizu, K. Uemura, H. Matsuda, N. Miura, N. Yamazoe, Journal of The Electrochemical Society **137**(11), 3430-3433 (1990).

[86] M. Morcrette, P. Barboux, J. Perriere, T. Brousse, Solid State Ionics **112**(3-4), 249-254 (1998).

[87] A. Rougier, K. A. Striebel, S. J. Wen, E. J. Cairns, Journal of The Electrochemical Society **145**(9), 2975-2980 (1998).

[88] A. Rougier, K. A. Striebel, S. J. Wen, T. J. Richardson, R. P. Reade, E. J. Cairns, Applied Surface Science **134**(1-4), 107-115 (1998).

[89] C. Julien, E. Haro-Poniatowski, M. A. Camacho-Lopez, L. Escobar-Alarcon, J. Jimenez-Jarquin, Materials Science and Engineering B-Solid State Materials for Advanced Technology **72**(1), 36-46 (2000).

[90] D. Singh, W. S. Kim, V. Craciun, H. Hofmann, R. K. Singh, Applied Surface Science **197**, 516-521 (2002).

[91] D. Singh, Influence of microstructure on electrochemical properties of Li-Mn-O thin films, in Département des Matériaux. 2001, Ecole Polytechnique Fédéral de Lausanne: Lausanne. p. 184.

[92] M. Morcrette, P. Barboux, J. Perriere, T. Brousse, A. Traverse, J. P. Boilot, Solid State Ionics **138**(3-4), 213-219 (2001).

[93] M. Inaba, T. Doi, Y. Iriyama, T. Abe, Z. Ogumi, Journal of Power Sources, **81**, 554-557 (1999).

[94] A. Rougier, K. A. Striebe, S. J. Wen, T. J. Richerdson, R. P. Reade, E. J. Cairns, Applied Surface Science **134**, 107-115 (1998).

[95] C. M. Julien, M. Massot, Materials Science And Engineering B-Solid State Materials for Advanced Technology **100**(1), 69-78 (2003).

[96] R. Chromik, F. Beck, Electrochimica Acta **45**(14), 2175-2185 (2000).